



An Expanded Three Band Model to Monitor Inland Optically Complex Water Using Geostationary Ocean Color Imager (GOCI)

Yulong Guo^{1,2}, Changchun Huang^{3*}, Yunmei Li³, Chenggong Du⁴, Yuan Li⁵, Weiqiang Chen^{1,2}, Lingfei Shi^{1,2} and Guangxing Ji^{1,2}

¹College of the Resources and Environmental Sciences, Henan Agricultural University, Zhengzhou, China, ²Henan Engineering Research Center of Land Consolidation and Ecological Restoration, Henan Agricultural University, Zhengzhou, China, ³School of Geography, Nanjing Normal University, Nanjing, China, ⁴Jiangsu Collaborative Innovation Center of Regional Modern Agriculture and Environmental Protection, Huaiyin Normal University, Huai'an, China, ⁵School of Tourism and Urban and Rural Planning, Zhejiang Gongshang University, Hangzhou, China

OPEN ACCESS

Edited by:

Minwei Zhang,
Science Applications International
Corporation, United States

Reviewed by:

Maycira Costa,
University of Victoria, Canada
Jun Zhao,
Sun Yat-sen University, China

*Correspondence:

Changchun Huang
huangchangchun@njnu.edu.cn

Specialty section:

This article was submitted to
Multi- and Hyper-Spectral Imaging,
a section of the journal
Frontiers in Remote Sensing

Received: 28 October 2021

Accepted: 01 March 2022

Published: 17 March 2022

Citation:

Guo Y, Huang C, Li Y, Du C, Li Y,
Chen W, Shi L and Ji G (2022) An
Expanded Three Band Model to
Monitor Inland Optically Complex
Water Using Geostationary Ocean
Color Imager (GOCI).
Front. Remote Sens. 3:803884.
doi: 10.3389/frsen.2022.803884

Due to strict spectral band requirements, the three-band (TB) chlorophyll-a concentration (C_{Chla}) estimation algorithm cannot be applied to GOCI image, which has great potential in frequently monitoring inland complex waters. In this study, the TB algorithm was expanded and applied to GOCI data. The GOCI TB algorithm was subsequently calibrated using an *in-situ* dataset which contains 281 samples collected from 17 inland lakes in China between 2013 and 2020. MERIS TB and GOCI band ratio (BR) models were selected as comparisons to assess the proposed model. The results showed that the proposed GOCI TB model has similar accuracy with MERIS TB model and overperformed GOCI BR model. The root mean square error (RMSE) of the GOCI TB, MERIS TB, and GOCI BR algorithms are 14.212 $\mu\text{g/L}$, 12.096 $\mu\text{g/L}$, and 20.504 $\mu\text{g/L}$, respectively. The mean absolute percentage error (MAPE) (when C_{Chla} is larger than 10 $\mu\text{g/L}$) of the three models were 0.377, 0.250, and 0.453, respectively. Similar conclusion could be drawn from a match-up dataset containing 40 samples. Finally, a simulation experiment was carried out to analyze the robustness of the models under various total suspended matter concentration (C_{TSM}) conditions. Both the *in-situ* validation and simulation experiment indicated that the GOCI TB factor could effectively eliminate the optical influence of C_{TSM} . Furthermore, the broader spectral range requirement of GOCI TB model made it proper for many other multispectral sensors such as Sentinel two Multispectral Instrument (S2 MSI), Moderate Resolution Imaging Spectroradiometer (MODIS) (onboard the Terra/Aqua satellite), and Visible Infrared Imaging Radiometer Suite (VIIRS) (onboard the National Polar-orbiting Partnership satellite). Compared with the GOCI BR algorithm, the GOCI TB algorithm has stronger stability, better accuracy, and greater potential in practice.

Keywords: three band model, C_{Chla} estimation, water color, GOCI, optically complex water

1 INTRODUCTION

C_{chla} , a basic indicator of phytoplankton biomass, has been widely used to indicate trophic status and water quality in oceans and inland waters (Honeywill et al., 2002; Lee et al., 2011; Neil et al., 2019). Remote estimate C_{chla} based on satellite sensor in large aquatic ecosystem provides numerous advantages compared with standard field measurements (Kutser, 2004). C_{chla} can be estimated using remote sensing data based on its unique spectral properties (Bresciani et al., 2011; Huang et al., 2014; Kravitz et al., 2019; Liu et al., 2020). But such estimates present difficulties for optically complex water bodies. Dall'Olmo and Gitelson (Dall'olmo and Gitelson, 2005; Dall'olmo and Gitelson, 2006) developed and validated a semi-analytical TB algorithm to estimate C_{chla} of optical complex inland water. The TB algorithm has been verified in different study areas (Zimba and Gitelson, 2006; Gitelson et al., 2007; Xu et al., 2009; Gurlin et al., 2011; Yacobi et al., 2011; Moses et al., 2012; Augusto-Silva et al., 2014; Huang et al., 2014), and improved by researchers (Le et al., 2009; Duan et al., 2010; Yang et al., 2010; Chen et al., 2013). However, due to its strict band requirements, the algorithm has only been successfully applied on hyperspectral image (Moses et al., 2012; Moses et al., 2014) and some narrow-band ocean color remote sensors such as the MEdium Resolution Imaging Spectrometer (MERIS) (Shi et al., 2013; Augusto-Silva et al., 2014; Huang et al., 2014) and Sentinel-3 Ocean and Land Colour Instrument (S3 OLCI) (Liu et al., 2020).

GOCI is the world's first geostationary ocean color multispectral system, with medium spatial resolution (500 m) and very high temporal resolution (1 h). Its high frequency refresh rate provides great potential for inland complex water monitoring (Huang et al., 2015a; Guo et al., 2020). However, in previous studies of remotely estimate of C_{chla} using GOCI images,

researchers tend to use empirical models such as BR model, with indistinct mechanisms (Huang et al., 2014; Bao et al., 2015; Huang et al., 2015b). For GOCI data, an accurate and explainable C_{chla} estimation algorithm is urgently needed.

In this study, two questions are addressed. First, could the GOCI BR algorithm correctly describe C_{chla} patterns in optically complex inland waters? Then, is there a clear theory foundation to apply the TB algorithm to GOCI? Focusing on these two questions, the objectives of this paper are 1) extend the TB model to make it proper for GOCI images; 2) calibrate and validate the proposed model in highly turbid inland waters in China using a dataset covering a long time series and a large spatial scale; and 3) assess the robustness and potential of the proposed model.

2 MATERIALS AND METHODS

2.1 In-situ Data

Field measurements from 12 cruises, including 281 points, were conducted to calibrate and validate the TB and BR algorithms. The sampling areas covered several turbid productive inland waters in China (Figure 1), including Hongze Lake, Taihu Lake, Dongting Lake, Datong Lake, Changhu Lake, Honghu Lake, Huanggai Lake, Wushan Lake, Poyang Lake, Liangzi Lake, Huangda Lake, and Cihu Lake. The sampling stations are illustrated in Figure 1 and their associate details are listed in Table 1. All measurements and water samples were obtained within 6 h of solar noon (13:00 GMT +8). At each station, the following parameters were measured: remote sensing reflectance ($R_{\text{rs}}(\lambda)$, sr^{-1}), C_{chla} , C_{TSM} , and absorption of phytoplankton ($a_{\text{ph}}(\lambda)$). In 281 samples, 188 of them were randomly selected as calibration dataset and the left 93 samples were used to validate the performance of the C_{chla} estimation models.

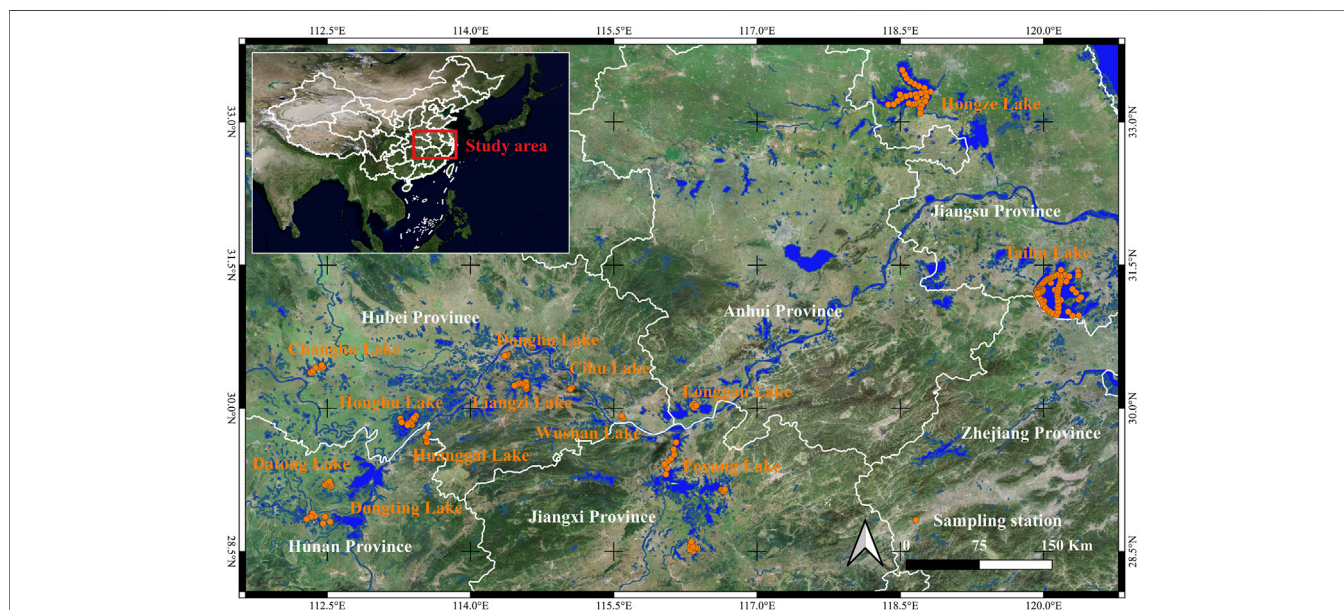


FIGURE 1 | Locations of the study area and distribution of the sampling stations.

TABLE 1 | Summary statistics of water parameters, including the concentrations of $C_{chl a}$ ($\mu\text{g/L}$), C_{TSM} (mg/L), and $a_{ph}(675)$ (m^{-1}), of all 17 cruises.

Lake	Samples	$C_{chl a}$ ($\mu\text{g/L}$)	C_{TSM} (mg/L)	$a_{ph}(675)$ (m^{-1})
Hongze Lake (Apr. 2019)	25	10.06 \pm 6.85	26.21 \pm 11.30	0.16 \pm 0.08
Hongze Lake (Jan. 2020)	24	17.91 \pm 5.84	39.10 \pm 14.71	0.44 \pm 0.10
Taihu Lake (Aug. 2013)	25	42.58 \pm 24.79	68.84 \pm 48.64	—
Taihu Lake (Nov. 2020)	31	20.88 \pm 3.72	23.66 \pm 16.49	—
Taihu Lake (Aug. 2016)	18	46.65 \pm 29.27	75.57 \pm 37.19	—
Taihu Lake (Mar. 2017)	44	31.19 \pm 10.70	73.68 \pm 30.54	0.48 \pm 0.22
Taihu Lake (Aug. 2019)	57	40.87 \pm 12.80	36.78 \pm 17.56	—
Dongting Lake (Jan. 2018)	8	0.78 \pm 0.25	7.69 \pm 6.31	—
Datong Lake (Jan. 2018)	6	4.75 \pm 1.70	—	—
Changhu Lake (Jan. 2018)	6	6.43 \pm 5.31	42.32 \pm 10.30	—
Honghu Lake (Jan. 2018)	8	8.99 \pm 4.03	12.83 \pm 8.14	—
Huanggai Lake (Jan. 2018)	5	69.51 \pm 19.72	18.68 \pm 9.72	—
Wushan Lake (Jan. 2018)	2	3.74 \pm 0.56	45.80 \pm 24.66	—
Poyang Lake (Jan. 2018)	9	2.21 \pm 0.66	3.15 \pm 1.86	—
Liangzi Lake (Jan. 2018)	7	0.97 \pm 0.47	13.63 \pm 5.54	—
Huangda Lake (Jan. 2018)	4	8.82 \pm 1.33	3.00 \pm 1.21	—
Cihu Lake (Jan. 2018)	2	30.51 \pm 0.21	6.44 \pm 2.99	—

The *in-situ* measured R_{rs} and $C_{chl a}$ were used for model calibration and validation. *In-situ* measured C_{TSM} was used to discuss the sensitivity of the models.

2.1.1 Measurement of R_{rs}

$R_{rs}(\lambda)$ measurements were conducted by means of an ASD FieldSpec spectroradiometer, which has a spectral range of 350–1,050 nm at increment of 1.5 nm. The spectral resolution was interpolated into 1 nm after measurement. According to the above-water measurement method described in the Ocean Optical Protocols (Mueller et al., 2003), the above-water measurement method was used to measure the radiance spectra of the reference panel, water, and sky, respectively. At each site, ten spectra were collected, from which abnormal ones were eliminated and valid ones retained and averaged. Specific observation geometry was applied to effectively avoid the interference of a ship with the water surface and the influence of direct solar radiation during the measurement (Tang et al., 2004). Finally, $R_{rs}(\lambda)$ was derived via the following equation (Tang et al., 2004; Le et al., 2009)

$$R_{rs}(\lambda) = (L_t - r \times L_{sky}) / (L_p \times \pi / \rho_p) \quad (1)$$

Where L_t is the total radiance received from the water surface; L_{sky} is the radiance from sky; L_p is the simultaneously observed radiance of the reference gray board. In this process, skylight reflectance at the air-water surface (r) was taken as 2.2% for calm weather, 2.5% for wind speed of up to 5 ms^{-1} , and 2.6–2.8% for wind speed of about 10 ms^{-1} (Tang et al., 2004). The reflectance of the gray diffuse board (ρ_p) had been accurately corrected to be 30% in the factory, before we used it to carry out these field experiments.

2.1.2 Measurement of Water Constituents' Concentration

Water samples were collected from the water surface (<20 cm) and kept in a cooler with ice. The fraction of each sample was used

to measure concentrations of water constituents. Water samples were filtered through 0.7 μm Whatman GF/F glass fibre filters that had been combusted at 550°C for 4 h. The glass fibre filters were dried at 105°C for 4 h. C_{TSM} was obtained by measuring the difference in weights between combusted and dried glass fibre filters. Water samples for measuring $C_{chl a}$ were filtered with GF/C filters (Whatman). Chlorophyll-a was extracted with ethanol (90%) at 80°C for 6 h in darkness and then analyzed spectrophotometrically at 750 and 665 nm with a correction for phaeopigments using a spectrophotometer (Shimadzu UV-3600) (Chen et al., 2006).

2.1.3 Measurement of $a_{ph}(\lambda)$

The water samples were filtered and analyzed by a spectrophotometer (Shimadzu UV-3600) to obtain $a_{ph}(\lambda)$ using the quantitative filter technique (Cleveland and Weidemann, 1993). First, the water samples were filtered through GF/C (Whatman) glass fibre filters to obtain TSM, and the absorbance of TSM was measured using a spectrophotometer. Pigments were removed from the water samples with NaClO and the water samples were refiltered to obtain tripton. The absorbance of tripton was obtained from these glass fibre filters using a spectrophotometer. Data processing to calculate $a_{ph}(\lambda)$ from the absorbance of tripton and TSM, respectively, was performed as described by Huang et al. (2011).

2.2 Satellite Data

Level-1b GOCI images covering Taihu Lake and Hongze Lake were downloaded from the Korea Ocean Satellite Centre (<http://kosc.kordi.re.kr/>). For the algorithm validation, the sampling times for the *in-situ* match-up data were ± 0.5 h for the GOCI transit time. There were 40 match-up points (11 from Taihu Lake, Aug. 2013, five from Taihu Lake, Aug. 2019, 10 from Hongze Lake, Apr. 2019, and 14 from Hongze Lake, Nov. 2020) for GOCI images. These images were vector masked to remove land and islands after geometric correction. The GOCI atmospheric correction was carried out using an improved land

target-based atmospheric correction method (Guanter et al., 2010; Liu et al., 2015).

2.3 Expanding of the TB Algorithm

The TB algorithm that developed by Dall'Olmo and Gitelson (Dall'olmo and Gitelson, 2005; Dall'olmo and Gitelson, 2006) is based on the following relationship between C_{chla} and R_{rs} :

$$C_{\text{chla}} \propto [R_{\text{rs}}^{-1}(\lambda_1) - R_{\text{rs}}^{-1}(\lambda_2)] \times R_{\text{rs}}(\lambda_3) \quad (2)$$

where R_{rs} is a function of the inherent absorption ($a(\lambda)$) and scattering ($b_b(\lambda)$) properties of the medium, according to the basic radiative transfer equation (Gordon et al., 1988).

$$R_{\text{rs}}(\lambda) = \frac{ft}{Qn^2} \frac{b_b(\lambda)}{a(\lambda) + b_b(\lambda)} \quad (3)$$

Absorption $a(\lambda)$ can be separated into absorption related to a_{ph} , a_{d} , a_{CDOM} , and pure water (a_w), while $b_b(\lambda)$ is the measurement of total backscattering. f/Q is depended on Sun zenith angle (Morel and Gentili, 1993), and can be approximated to be 0.0945 (Gordon et al., 1988), and $t/n^2 = 0.54$ (Austin, 1974; Clark, 1981).

The difference between the reciprocal reflectance $R^{-1}(\lambda_1)$ and $R^{-1}(\lambda_2)$ is approximated by

$$R_{\text{rs}}^{-1}(\lambda_1) - R_{\text{rs}}^{-1}(\lambda_2) \propto \frac{a_{\text{ph}}(\lambda_1) + a_w(\lambda_1) - a_w(\lambda_2)}{b_b} \quad (4)$$

based on the following assumptions: (a) b_b is spectrally invariant between λ_1 and λ_2 ; (b) $a_{\text{ph}}(\lambda_1) \gg a_{\text{ph}}(\lambda_2)$; (c) $a_{\text{d}}(\lambda_1) + a_{\text{CDOM}}(\lambda_1) \approx a_{\text{d}}(\lambda_2) + a_{\text{CDOM}}(\lambda_2)$.

Then, the third band, λ_3 is included to remove the effect of b_b . λ_3 is chosen to be in the near infrared (NIR) wavelengths, where reflectance by a_{ph} , a_{d} , and a_{CDOM} is minimal:

$$R_{\text{rs}}(\lambda_3) \propto \frac{b_b(\lambda_3)}{a(\lambda_3) + b_b(\lambda_3)} \approx \frac{b_b}{a_w(\lambda_3)} \propto b_b \quad (5)$$

The a_{ph} could be extracted by combining Eqs 4, 5:

$$[R_{\text{rs}}^{-1}(\lambda_1) - R_{\text{rs}}^{-1}(\lambda_2)] \times R_{\text{rs}}(\lambda_3) \propto C_{\text{chla}} \quad (6)$$

Eq. 6 is the basic formula of the traditional TB algorithm, where λ_1 is in the spectral region in which chlorophyll-a shows maximum absorbance ($\lambda_1 = 660\text{--}690$ nm). λ_2 is in the spectral region in which chlorophyll-a shows minimum absorbance. The absorption of tripton and CDOM at λ_2 are very close to those at λ_1 ($\lambda_2 = 700\text{--}730$ nm). λ_3 is located in the spectral region such that $R_{\text{rs}}(\lambda_3)$ is minimally affected by absorption of water constituents ($\lambda_3 = 740\text{--}760$ nm). Therefore, in multispectral sensors, only thin-band multispectral sensors like MERIS and S3 OLCI were widely used. According to the previous description, MERIS centre wavelengths for TB algorithm are $\lambda_1 = 681$ nm, $\lambda_2 = 708$ nm, and $\lambda_3 = 753$ nm. To simplify the discussion, Eq. 6 could be written as:

$$[R^{-1}(681) - R^{-1}(708)] \times R(753) \propto C_{\text{chla}} \quad (7)$$

According to some previous studies (Smyth et al., 2006; Chen et al., 2014), the ratio of absorption in different wavelength is fixed:

$$\varepsilon_a(\lambda_1, \lambda_2) = a(\lambda_1)/a(\lambda_2) \quad (8)$$

What's more, the GOCI band five is located in 660 nm (Table 1), which is nearby band 6 (680 nm). Then, the following equation can be established:

$$a_{\text{ph}}(680) = \varepsilon_{\text{aph}}(680, 660) \times a_{\text{ph}}(660) \quad (9)$$

Therefore, the position of λ_2 in the standard TB algorithm could be moved from 710 to 660 nm to fit the GOCI band setting. Eq. 4 could be written as:

$$R^{-1}(680) - R^{-1}(660) \propto \frac{(\varepsilon_{\text{aph}}(680, 660) - 1) \times a_{\text{ph}}(660) + a_w(680) - a_w(660)}{b_b} \quad (10)$$

Then, the expanded TB algorithm could be expressed as the following equation by combing Eq. 5 and Eq. 10 in the assumption that $\varepsilon_{\text{aph}}(680, 660)$ is fixed:

$$[R_{\text{rs}}^{-1}(680) - R_{\text{rs}}^{-1}(660)] \times R_{\text{rs}}(745) \propto C_{\text{chla}} \quad (11)$$

2.4 Accuracy Assessment

MAPE and RMSE were used to indicate errors in the estimated values, which could be calculated through the following equations:

$$\text{RMSE} = \sqrt{\frac{\sum_{i=1}^n (y_i - y'_i)^2}{n}} \quad (12)$$

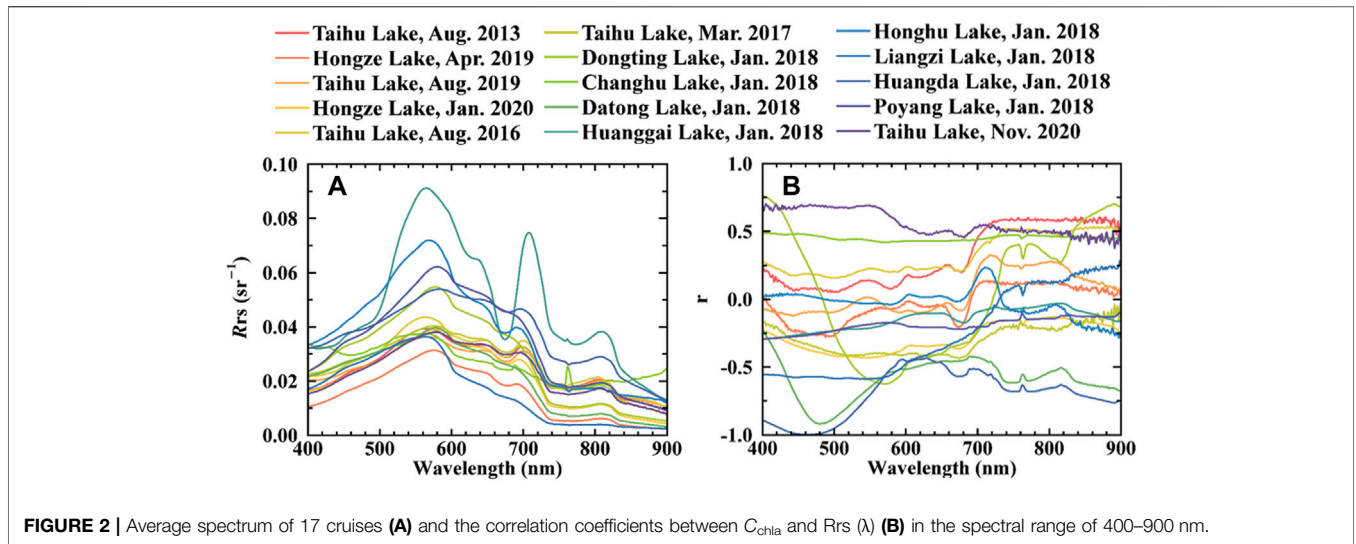
$$\text{MAPE} = \frac{1}{n} \sum_{i=1}^n \left| \frac{y_i - y'_i}{y_i} \right| \quad (13)$$

Where n is the number of samples; y_i is the measured value; y'_i is the estimated value. In practical, MAPE indexes under different C_{chla} levels fluctuated dramatically. To better reflect the model performance, MAPE_{low} (only the samples that measured C_{chla} less than 10 $\mu\text{g/L}$ were included) and MAPE_{high} (only the samples that measured C_{chla} greater or equal to 10 $\mu\text{g/L}$ were included) were calculated separately.

2.5 Simulation Experiment

The main theoretical advantage of TB model is it will eliminate the optical influence of C_{TSM} in NIR spectral range. Therefore, we analyzed this influence based on a bio-optical model calibrated by Huang et al. (2011). In the bio-optical model, R_{rs} was expressed as a function of C_{TSM} , C_{chla} , and $a_{\text{CDOM}}(\lambda_0)$ (Appendix A). To reveal the influence of C_{TSM} to C_{chla} estimation models, we simulated R_{rs} spectra between 400 and 800 nm under different C_{chla} and C_{TSM} combinations. C_{chla} and C_{TSM} were ranging from 1 $\mu\text{g/L}$ to 200 $\mu\text{g/L}$, and 1 mg/L to 200 mg/L, respectively. $a_{\text{CDOM}}(\lambda_0)$ was set to 0.5. Then, we defined a variable named model factor difference (Δ factor) to evaluate the stability of model factors to C_{TSM} . The expression of Δ factor is as follows:

$$\Delta_{\text{factor}}(C_{\text{chla}}, C_{\text{TSM}}) = \text{factor}(C_{\text{chla}}, C_{\text{TSM}}) - \text{factor}(C_{\text{chla}}, 1) \quad (14)$$



where *factor* represents the three $C_{chl a}$ model factors, that is, MERIS TB (MTB) factor (i.e., $[R^{-1} rs(681) - R^{-1} rs(708)] R_{rs}(753)$), GOCI TB (GTB) (i.e., $[R^{-1} rs(680) - R^{-1} rs(660)] R_{rs}(745)$) factor, and GOCI BR (GBR) factor (i.e., $R_{rs}(745)/R_{rs}(680)$). All the factors were calculated from R_{rs} at a specific $C_{chl a}$ and C_{TSM} level. Δ factor represents the stability of the current factor to C_{TSM} . A Δ factor close to 0 means the current factor is not sensitive to C_{TSM} at the current $C_{chl a}$ level.

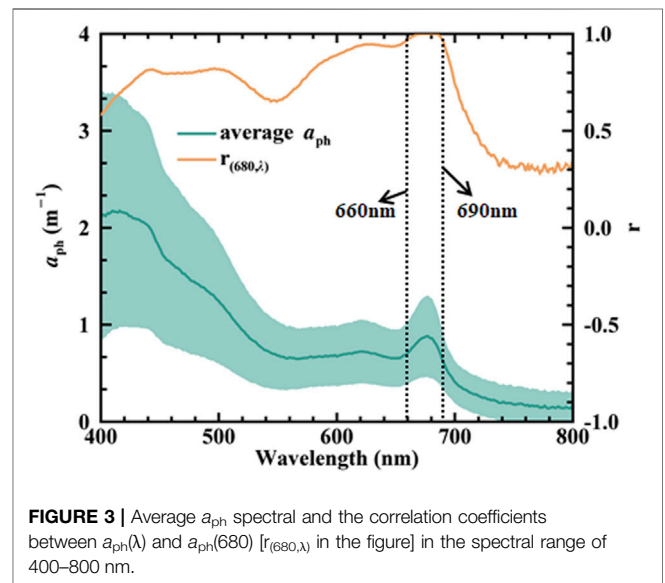
3 RESULTS

3.1 R_{rs} Spectra Characteristics

The average R_{rs} (Figure 2A) of 15 cruises exhibited wide variability in terms of both magnitude and shape. Spectra of Wushan Lake and Cihu Lake were not plotted because we only collected two samples in these two lakes. This is inadequate to generate the correlation line. For eutrophic water, such as Huanggai Lake (Jan. 2018) and Taihu Lake (Aug. 2016), strong phytoplankton absorption formed the R_{rs} peaks around 570, 700, and 815 nm, and the trough near 675 nm. For some other cruises such as Changhu Lake (Jan. 2018), its high turbidity and light eutrophication determined the stronger reflectance in red spectral range and weaker trough near 675 nm (Figure 2A). For relatively clean waters that contain less C_{TSM} and $C_{chl a}$, like Liangzi Lake (Jan. 2018), the average R_{rs} curve have small magnitude and weak phytoplankton characters in red and NIR spectral ranges.

The correlation coefficients between R_{rs} and $C_{chl a}$ at each wavelength (Figure 2B) also indicated the complexity of the samples. Datasets with significant trough at 680 nm and peak at 700 nm exhibited similar correlation curves. However, for lakes with high turbidity and low eutrophication level, like Changhu Lake, the correlation line looks flat: peak in 700 nm disappeared because high turbidity weakened the R_{rs} sensitivity to $C_{chl a}$.

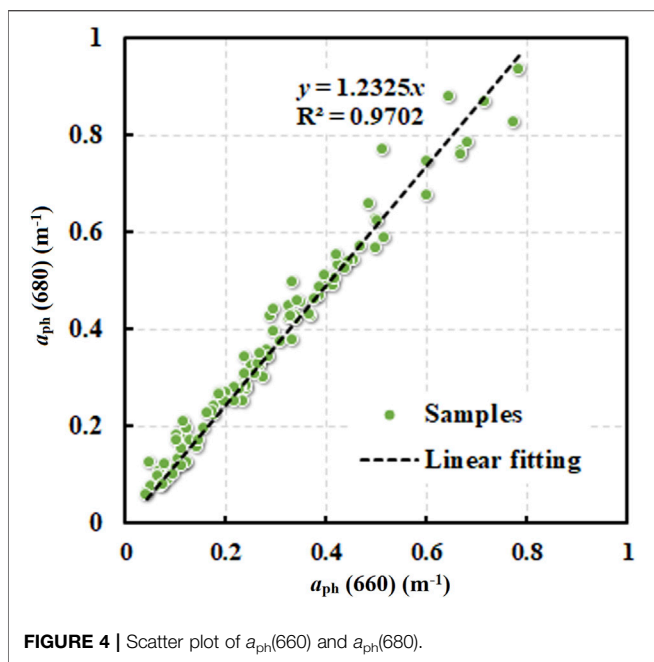
In conclusion, the complex optical properties of inland water require a $C_{chl a}$ estimation model that could eliminate the optical influence of other water color constituents, especially C_{TSM} .



3.2 a_{ph} Spectra Characteristics

The average a_{ph} spectrum (Figure 3) contains three peaks. The first one is at 440 nm, which is caused by chlorophyll-a, chlorophyll-b, chlorophyll-c, carotenoid, and other accessory pigments. The second peak at 625 nm is caused by phycocyanin. The last one around 675 nm is mainly caused by the absorption of chlorophyll-a (Haardt and Maske, 1987; Dekker, 1993).

In order to investigate the rationality of the core assumption of the GOCI TB model, i.e., the stability of ϵ_{aph} , we calculated linear correlation coefficients between a_{ph} at 680 nm and other spectral bands (i.e., line $r_{(680,\lambda)}$ in Figure 3). Overall, the $r_{(680,\lambda)}$ line had a similar shape with the average a_{ph} line. This means the main factor that affects inter-band correlation of a_{ph} is its magnitude. In detail, the relationship became stronger in the spectral range from 400 to 500 nm. Then, a trough appears in 550 nm. In



the wavelength range between 600 and 690 nm, $r_{(680, \lambda)}$ is entirely greater than 0.9. The strongest correlation appears in 660–690 nm, where the $r_{(680, \lambda)}$ line is above 0.98. For the bands beyond 690 nm, with the increasing of wavelength, the correlation coefficients rapidly decrease together with the a_{ph} spectrum.

The relationship between $a_{ph}(660)$ and $a_{ph}(680)$ (Figure 4) of all the available *in-situ* samples denote that when the intercept is set to 0, the linear fitting R^2 is 0.965. This means $a_{ph}(660)$ can explain more than 96% changes of $a_{ph}(680)$ in our dataset. Therefore, the assumption in Eq. 9, i.e., $\epsilon_{aph}(680,660)$ is fixed, is considered to be reasonable in this study ($\epsilon_{aph}(680,660) = 1.23$).

3.3 Calibration and Validation of the Models

Three algorithms were calibrated and validated in this study, they are: MERIS TB algorithm (based on Eq. 7), GOCI TB algorithm (based on Eq. 11), and GOCI BR algorithm $R_{rs}(745)/R_{rs}(680)$ (Huang et al., 2014; Bao et al., 2015) was selected as the model factor. The whole *in-situ* dataset was randomly separated into 188 calibration samples and 93 validation samples. The parameters of the three models were determined in the calibration dataset by a simple linear fitting method (Figures 5A,C,E). Their expressions are as follows:

$$C_{chla} = 260.850 \times [R_{rs}^{-1}(681) - R_{rs}^{-1}(708)]R_{rs}(753) + 26.342 \quad (R^2 = 0.878, P < 0.001) \quad (15)$$

$$C_{chla} = 763.230 \times [R_{rs}^{-1}(680) - R_{rs}^{-1}(660)]R_{rs}(745) - 4.485 \quad (R^2 = 0.823, P < 0.001) \quad (16)$$

$$C_{chla} = 127.940 \times \frac{R_{rs}(745)}{R_{rs}(680)} - 35.436 \quad (R^2 = 0.569, P < 0.001) \quad (17)$$

In the validation dataset, RMSE of the MERIS TB, GOCI TB, and GOCI BR models are 12.943 $\mu\text{g/L}$, 13.313 $\mu\text{g/L}$, and 22.613 $\mu\text{g/L}$, respectively. MAPE_{low} samples are 8.089, 7.725, and 29.898, respectively. MAPE_{high} are 0.433, 0.463, and 0.915, respectively (Figures 5B,D,F). The results indicated that GOCI TB algorithm performs better than GOCI BR algorithm and similar with MERIS TB algorithm. Wavelengths in the brackets represent specific band centers of MERIS and GOCI.

3.4 Performance in Match-Up Samples

Table 2 shows the atmospheric correction results of the 40 match-up points. The average MAPE and RMSE over all spectral bands are 0.216 and 4.578×10^{-3} , respectively. Generally, the atmospheric correction yields satisfactory accuracy, especially for red and NIR bands.

The C_{chla} estimation results from GOCI TB and BR models represent that, generally, the performance of the two models are similar with those of *in-situ* dataset (Figure 5). RMSE of BR and TB models are 12.42 $\mu\text{g/L}$ and 9.90 $\mu\text{g/L}$, respectively. This means that GOCI TB model improved the accuracy for about 25%. MAPE of BR and TB models are 0.94 and 0.60, respectively. The improvement was about 56%. This suggesting that the GOCI TB model could improve more estimation accuracy in low C_{chla} conditions.

3.5 C_{chla} Maps

We applied GOCI TB and BR models to the preprocessed GOCI images and yielded the C_{chla} maps (Figure 6). Generally, the GOCI TB and GOCI BR C_{chla} maps have similar spatial distribution: high C_{chla} values appeared in Zhushan Bay, Meiliang Bay, north of Gonghu Bay, and south west lake. Low C_{chla} region distributed in the center lake. Notably, an opposite trend appeared between GOCI TB C_{chla} series and GOCI BR C_{chla} series: from 8:30 to 15:30, C_{chla} is getting larger in GOCI TB C_{chla} maps and smaller in the GOCI BR yielded ones.

4 DISCUSSION

4.1 Error Distribution Analysis

TB model can eliminate the optical influence of total suspended matter in NIR spectral range. To visualize this elimination, MAPE of each sample was calculated for all the three models and plotted in the C_{chla} - C_{TSM} space (Figure 7). The results indicated that, generally, MERIS TB and GOCI TB have similar MAPE distribution. GOCI TB algorithm performs slightly better in low C_{chla} ($C_{chla} < 10 \mu\text{g/L}$), high C_{TSM} ($C_{TSM} > 30 \text{ mg/L}$) region, where GOCI BR result exhibits significant error (Figure 5E and Figure 7C).

To understand the failure of the GOCI BR algorithm in low C_{chla} , high C_{TSM} condition, we carried out a further analysis. Based on GOCI band settings, the linear correlation coefficients of BR factor with both C_{chla} and C_{TSM} were calculated (Figure 8). What interesting is, the correlation map of C_{TSM} has a similar distribution with that of C_{chla} . Even the overall correlation coefficients of C_{TSM} are lower than C_{chla} , the significant correlation between BR factors and C_{TSM} at 680, 745, and 865 nm indicated the unneglectable influence of suspended matter in BR model. Meanwhile, the correlation coefficients

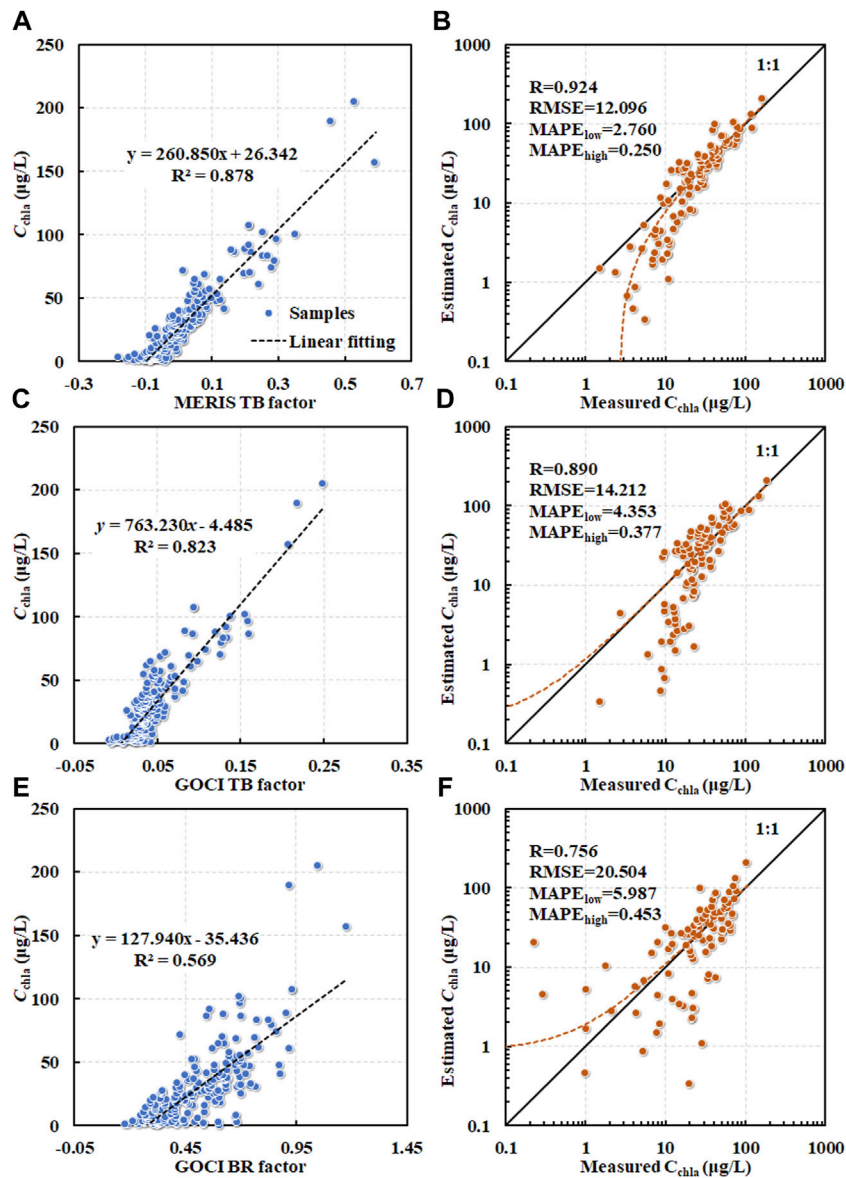


FIGURE 5 | Scatter plot of (A) MERIS TB model; (C) GOCI TB model; (E) GOCI BR model, and the validation result of (B) MERIS TB model; (D) GOCI TB model; (F) GOCI BR model.

TABLE 2 | Atmospheric correction errors.

Band	MAPE	RMSE(sr ⁻¹)
B412	0.423	8.030×10^{-3}
B443	0.239	6.146×10^{-3}
B490	0.127	4.436×10^{-3}
B555	0.127	5.550×10^{-3}
B660	0.140	4.393×10^{-3}
B680	0.133	3.862×10^{-3}
B745	0.238	2.528×10^{-3}
B865	0.301	1.677×10^{-3}
average	0.216	4.578×10^{-3}

between GOCI TB factors and C_{TSM} was 0.286, which is obviously lower than that of BR factors (higher than 0.5 in **Figure 8B**). This comparison suggesting that compared with GOCI BR factor, GOCI TB factor could effectively eliminate the impact of TSM and yield a more reliable $C_{chl a}$ estimation result.

4.2 Theoretical Analysis of the Model Sensitivity to C_{TSM}

The simulation experiment results will be discussed as follows: For each $C_{chl a}$ level, we calculated Δ_{factor} under all C_{TSM}

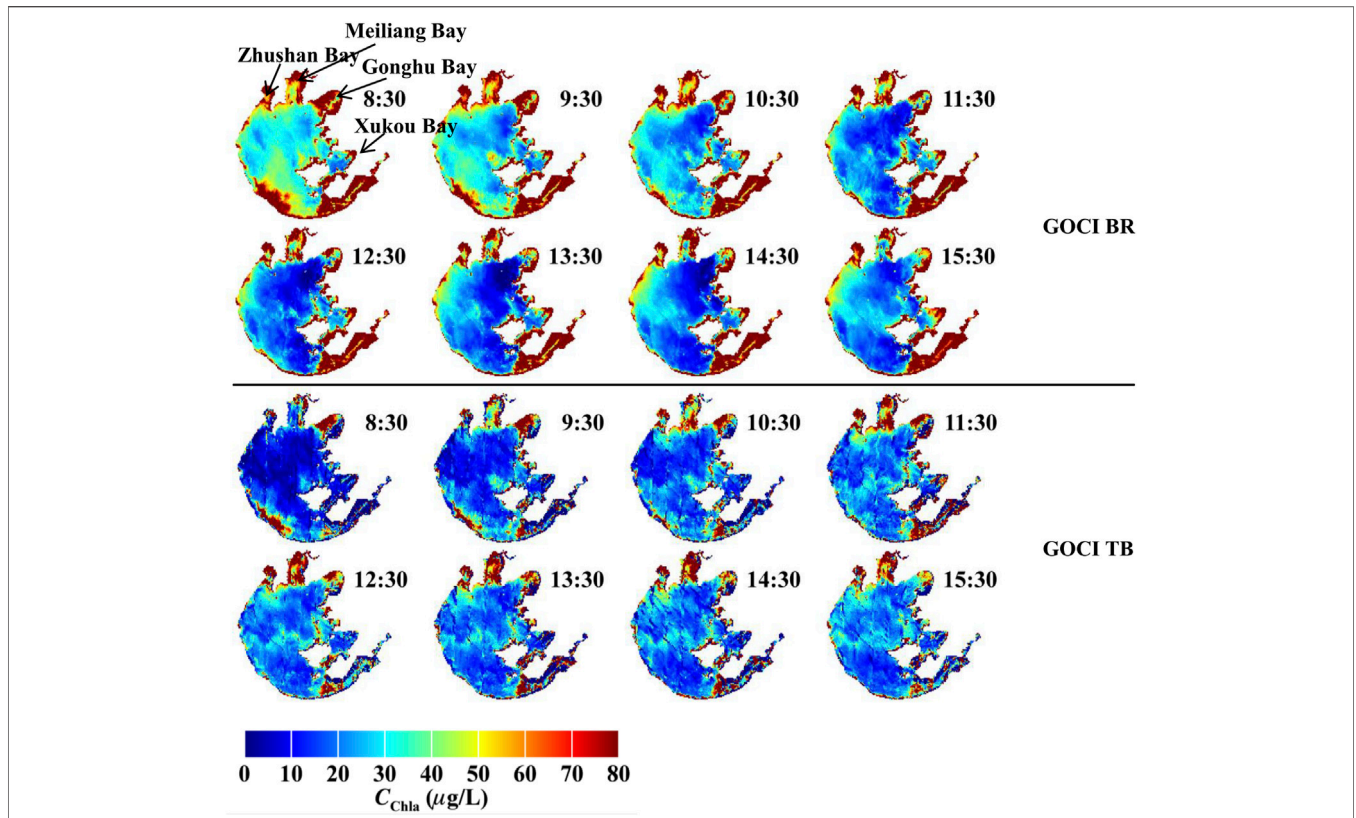


FIGURE 6 | $C_{chl a}$ maps that yielded by BR and TB algorithm using GOCI image in 13 May 2013.

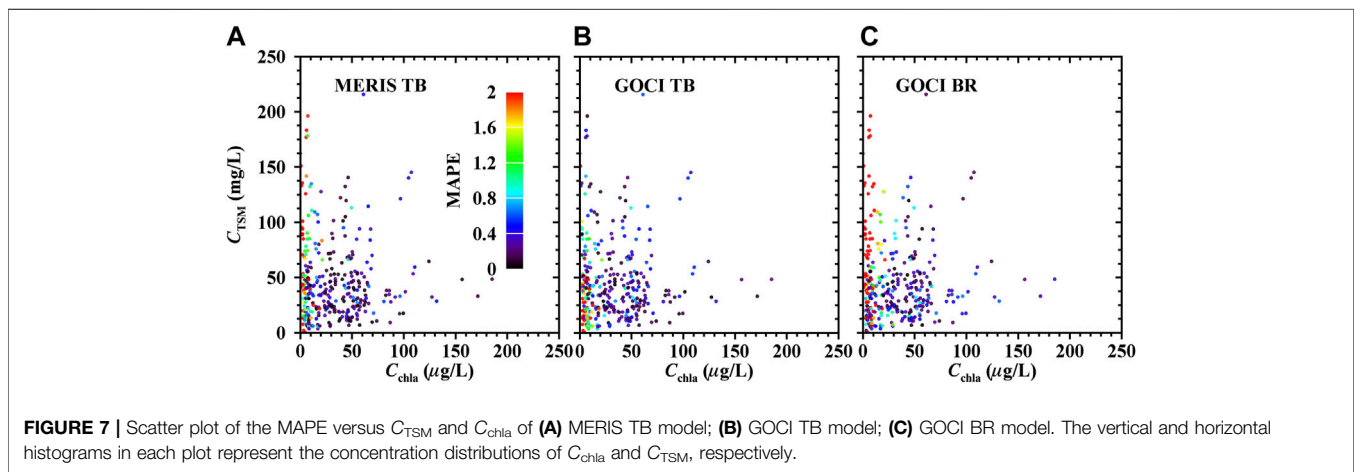


FIGURE 7 | Scatter plot of the MAPE versus C_{TSM} and $C_{chl a}$ of (A) MERIS TB model; (B) GOCI TB model; (C) GOCI BR model. The vertical and horizontal histograms in each plot represent the concentration distributions of $C_{chl a}$ and C_{TSM} , respectively.

conditions to yield a sensitivity line in **Figure 9**. For an ideal factor that could completely erase the impact of C_{TSM} , the sensitivity line will be $y = 0$ (the dashed lines in **Figure 9**), which means no matter how much TSM is in the water, the spectral factor kept the same. Therefore, the distance of Δ_{factor} line to the dashed line reflects the stability of the current factor.

The results (**Figure 9**) indicated that the three factors have different stable $C_{chl a}$ ranges. Generally, the influence of TSM to $C_{chl a}$ spectra factors are increasing together with C_{TSM} . However,

For MERIS TB factor, the most stable $C_{chl a}$ range is about $70 \mu\text{g/L}$ (**Figure 9B**). High $C_{chl a}$ sensitivity and low $C_{chl a}$ sensitivity lines equally distributed around the dashed line. GOCI TB factor is insensitive to C_{TSM} when $C_{chl a}$ is smaller than $40 \mu\text{g/L}$ (**Figure 9C**). With the increasing of C_{TSM} , offset of the high $C_{chl a}$ sensitivity line became larger. Δ GBR has a linear relationship with C_{TSM} . For lower $C_{chl a}$, the factor difference is higher, which indicates that the GOCI BR factor is unstable in low $C_{chl a}$ conditions.

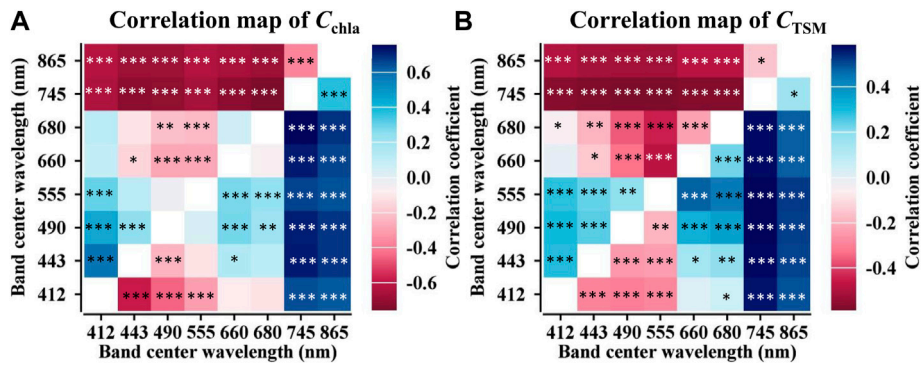


FIGURE 8 | Correlation maps of GOCI BR factors to (A) $C_{chl a}$ and (B) C_{TSM} . Marks “*”, “**”, and “***” represent for p value less than 0.05, 0.01, and 0.001, respectively.

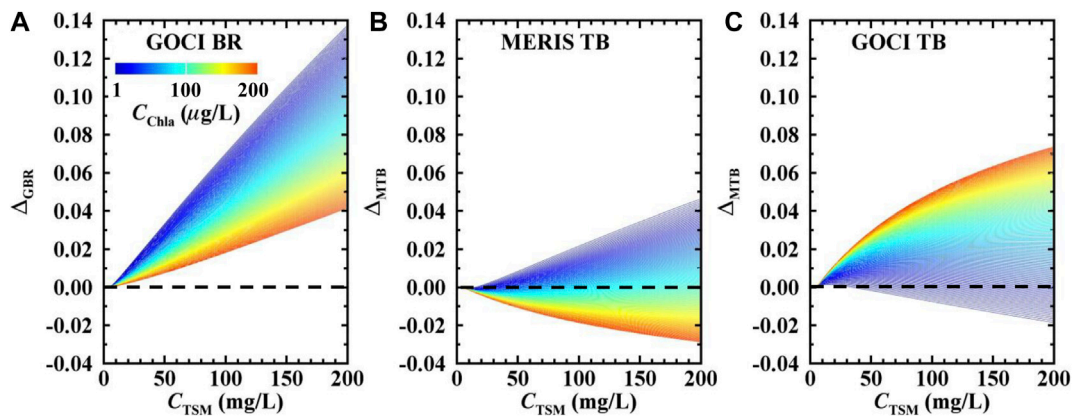


FIGURE 9 | Sensitivity simulation result of (A) GOCI BR model, (B) MERIS TB model, and (C) GOCI TB model in different C_{TSM} and $C_{chl a}$ conditions.

In conclusion, the MERIS TB and GOCI TB factors perform similar: they both have stable $C_{chl a}$ ranges, which are around 76 $\mu\text{g/L}$ and less than 40 $\mu\text{g/L}$, respectively. GOCI BR algorithm did not show a stable region: with the increasing of C_{TSM} , the factor became more and more sensitive to TSM. The simulation results can partly explain the model performances in section 4.1.

4.3 Comparison of $C_{chl a}$ Maps Yielded From GOCI TB and BR Models

Water constituents time series of specific water body has been widely reported (Le et al., 2013; Feng et al., 2014; Palmer et al., 2015). Meanwhile, we proved that different models have different performance under varied conditions (section 3.4). Then, how will this difference affect the spatial-temporal distribution of $C_{chl a}$ maps? To answer this question, we calculated the correlation coefficients between GOCI TB and BR yielded $C_{chl a}$ maps pixel by pixel (Figure 10A). A positive correlation coefficient denotes that $C_{chl a}$ yielded from TB and BR algorithms have similar temporal changes, and vice versa. The results indicated that in high $C_{chl a}$ regions, like Zhushan Bay, Meiliang Bay, Gonghu Bay, and south west lake, two map series showed strong consistency. The

correlation coefficients are generally higher than 0.8. However, a large negative correlation region in the center lake means that the two series have totally opposite $C_{chl a}$ trends in this region. C_{TSM} sensitivity discussed in section 4.2 can explain this phenomenon: resuspension in the center lake increased C_{TSM} and the instability of GOCI BR model. The histogram of correlation coefficient map (Figure 11B) demonstrated that the two models yielded opposite trends in a considerable region of Taihu Lake. This will definitely influence the statistical analysis in long-term water $C_{chl a}$ monitoring missions.

4.4 Influence of Position and Width of Band λ_2 to GOCI TB Model

Our expansion to the TB model is focusing on λ_2 . Following the original ideal of the TB model, we analyzed the effect of band λ_2 to the GOCI TB model by calculating the band-by-band correlation coefficients between $C_{chl a}$ and GOCI TB factor.

We fixed the positions of λ_1 and λ_3 and changed band λ_2 from 600 to 740 nm to yield the correlation coefficient line (Figure 11). The widest and highest correlation peak (the first peak in Figure 11) appears at around 710nm, where is close to the theoretical optimal

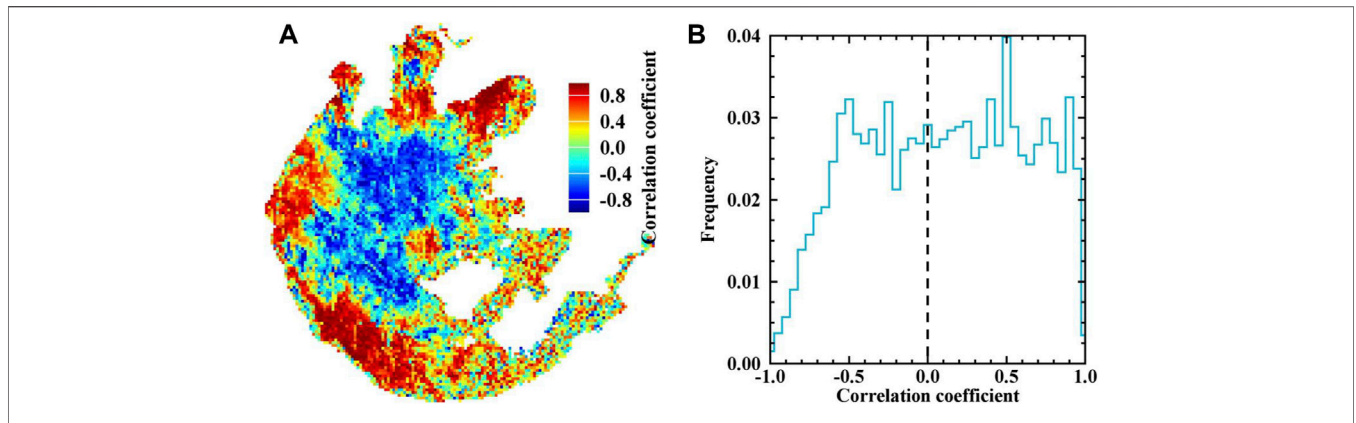


FIGURE 10 | Time series correlation coefficients between TB model and BR yielded $C_{chl a}$ maps (A), and its probability density plot (B).

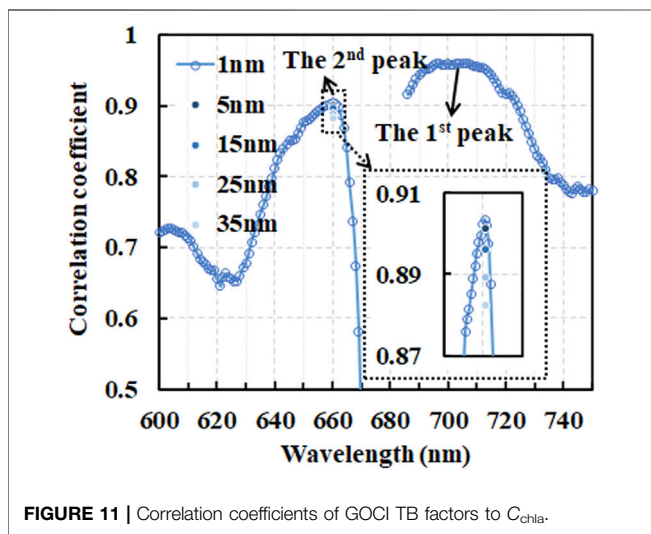


FIGURE 11 | Correlation coefficients of GOCI TB factors to $C_{chl a}$.

band position in previous researches (Dall’olmo and Gitelson, 2005; Le et al., 2011). Therefore, the first peak is the best choice when the sensor could provide proper spectral bands. It is also worth noting that the second peak exists at around 660 nm (Figure 11). In fact, this peak had been reported by Dall’olmo and Gitelson, 2005 and Le et al. (2009) researches. This suggesting that 660 nm is always a potential selection for TB models.

To further discuss the impact of bandwidth to the GOCI TB model, we resampled R_{rs} (660) to 5, 15, 25, and 35 nm width, respectively. Then, we calculated the GOCI TB factor based on the resampled R_{rs} (660) and their correlation coefficients with $C_{chl a}$ (Figure 11). The result denoted that, even the bandwidth was set to 35 nm, the GOCI TB factor still have high correlation coefficient with $C_{chl a}$ (larger than 0.87). This means that the GOCI TB factor is not sensitive to the width of band λ_2 .

4.5 Potential of the Expanded TB Algorithm

An obstacle of applying traditional TB algorithm is band λ_2 , which located in range of 690–710 nm (Dall’olmo and Gitelson,

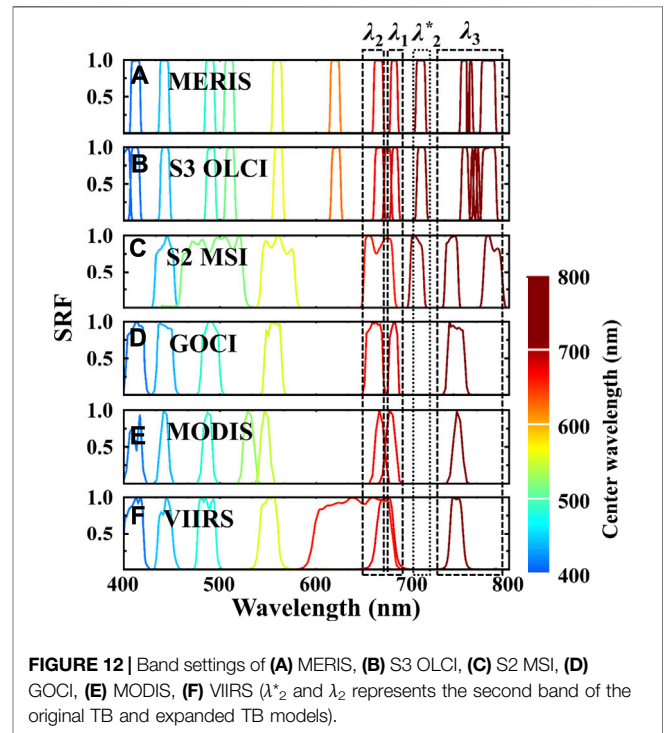


FIGURE 12 | Band settings of (A) MERIS, (B) S3 OLCI, (C) S2 MSI, (D) GOCI, (E) MODIS, (F) VIIRS (λ_2^* and λ_2 represents the second band of the original TB and expanded TB models).

2005; Dall’olmo and Gitelson, 2006). By a strict theoretical derivation, the expanded TB model suggests that when the sensor set no bands in 690–710 nm, λ_2 can be moved to 660–690 nm. The expanded TB algorithm has both clear mechanism and satisfactory performance. In fact, apart from GOCI, the proposed model can be also applied to multispectral sensors like S2 MSI, MODIS (onboard the Terra/Aqua satellite), and VIIRS (onboard the National Polar-orbiting Partnership satellite) (Figure 12).

Therefore, for MODIS (250/500 m band settings), VIIRS, and S2 MSI, their TB and best-fitted BR models were calibrated using the *in-situ* dataset (Table 3). In general, all the sensors perform better using TB model. Especially for MODIS and S2 MSI. For

TABLE 3 | TB and BR models for MODIS, VIIRS, and S2

Sensor	Variable	Model	RMSE ($\mu\text{g/L}$)	MAPE _{low}	MAPE _{high}
MODIS	$(R_{rs}^{-1}(675) - R_{rs}^{-1}(665)) \times R_{rs}(745)$	$1,182.400x - 0.211$ $R^2 = 0.813, \rho < 0.005$	15.299	4.145	0.370
	$R_{rs}(745)/(R_{rs}(675))$	$127.140x - 34.178$ $R^2 = 0.586, \rho < 0.005$	20.319	5.902	0.450
VIIRS	$(R_{rs}^{-1}(666) - R_{rs}^{-1}(640)) \times R_{rs}(746)$	$127.140x - 35.175$ $R^2 = 0.586, \rho < 0.005$	20.022	6.624	0.478
	$R_{rs}(746)/(R_{rs}(666))$	$126.510x - 32.030$ $R^2 = 0.511, \rho < 0.005$	21.972	6.439	0.455
S2 MSI	$(R_{rs}^{-1}(703) - R_{rs}^{-1}(665)) \times R_{rs}(739)$	$-332.340x + 27.294$ $R^2 = 0.866, \rho < 0.005$	13.175	2.932	0.253
	$R_{rs}(703)/(R_{rs}(665))$	$147.750x - 117.93$ $R^2 = 0.818, \rho < 0.005$	17.715	4.218	0.303

MODIS, compared with BR model, the TB model decreased the RMSE, MAPE_{low} and MAPE_{high} by 24.70%, 29.76%, and 17.77%. These reductions for S2 MSI are 25.62%, 30.48%, and 16.50%, respectively. For VIIRS, the band width of λ_2 is so broad (Figure 12) that it is partly out of the second high correlation peak (Figure 11). Even though, TB model still improved the performance slightly.

Conclusively, the expanded TB algorithm provides a wider choice for accurately monitoring inland complex water.

5 CONCLUSION

In this research, the TB algorithm is expanded for GOCI image to remotely estimate C_{chla} for optically complex water. The GOCI TB model was calibrated and validated by a comprehensive *in-situ* measured dataset and GOCI images. By comparing with MERIS TB and GOCI BR algorithms, the following conclusions can be drawn:

- 1) In the expanded TB algorithm, λ_2 is located in the spectral range between 680 and 700 nm or 660–680 nm. The core assumption of the expanded TB algorithm is reasonable. The validation result indicated that GOCI TB algorithm have similar accuracy with MERIS TB algorithm.
- 2) In highly turbid waters, GOCI BR factor cannot explain the change of C_{chla} . Meanwhile, the GOCI TB algorithm successfully eliminates b_b at NIR spectral range and performs well in high C_{TSM} conditions.

REFERENCES

- Augusto-Silva, P., Ogashawara, I., Barbosa, C., De Carvalho, L., Jorge, D., Fornari, C., et al. (2014). Analysis of MERIS Reflectance Algorithms for Estimating Chlorophyll-A Concentration in a Brazilian Reservoir. *Remote Sensing* 6, 11689–11707. doi:10.3390/rs61211689
- Austin, R. (1974). Inherent Spectral Radiance Signatures of the Ocean Surface. *Ocean color Anal.* 7410, 1–20.
- Bao, Y., Tian, Q., and Chen, M. (2015). A Weighted Algorithm Based on Normalized Mutual Information for Estimating the Chlorophyll-A Concentration in Inland Waters Using Geostationary Ocean Color Imager (GOCI) Data. *Remote Sensing* 7, 11731–11752. doi:10.3390/rs70911731

- 3) Compared with the BR algorithm, GOCI TB algorithm can yield more reasonable C_{chla} map for water environment monitoring and analyzing.
- 4) The expanded TB algorithm is proper for other multispectral sensors like S2 MSI, MODIS, and VIIRS. It provides wider choice for the future inland water remote monitoring missions.

DATA AVAILABILITY STATEMENT

The original contributions presented in the study are included in the article/Supplementary Material, further inquiries can be directed to the corresponding author.

AUTHOR CONTRIBUTIONS

YG performed the data and analysis. YG and CH wrote the paper. CH designed the research. YL, CD, and YL helped to design the experiments. WC contributed to the model development. LS and GJ helped to refine the algorithm.

FUNDING

This work is supported by National Natural Science Foundation of China (grant #: 41971286, 41701422, 42001296, 42071333) and Natural Science Foundation of Jiangsu Province (grant number BK20191058).

- Bresciani, M., Stroppiana, D., Odermatt, D., Morabito, G., and Giardino, C. (2011). Assessing Remotely Sensed Chlorophyll-A for the Implementation of the Water Framework Directive in European Perialpine Lakes. *Sci. Total Environ.* 409, 3083–3091. doi:10.1016/j.scitotenv.2011.05.001
- Chen, J., Cui, T., Qiu, Z., and Lin, C. (2014). A Three-Band Semi-analytical Model for Deriving Total Suspended Sediment Concentration from HJ-1A/CCD Data in Turbid Coastal Waters. *ISPRS J. Photogrammetry Remote Sensing* 93, 1–13. doi:10.1016/j.isprs.2014.02.011
- Chen, J., Quan, W., Wen, Z., and Cui, T. (2013). An Improved Three-Band Semi-analytical Algorithm for Estimating Chlorophyll-A Concentration in Highly Turbid Coastal Waters: a Case Study of the Yellow River Estuary, China. *Environ. Earth Sci.* 69, 2709–2719. doi:10.1007/s12665-012-2093-1

- Chen, Y., Chen, K., and Hu, Y. (2006). Discussion on Possible Error for Phytoplankton Chlorophyll-A Concentration Analysis Using Hot-Ethanol Extraction Method. *J. Lake Sci.* 18, 550–552.
- Clark, D. K. (1981). "Phytoplankton Pigment Algorithms for the Nimbus-7 CZCS," in *Oceanography from Space* (Springer), 227–237. doi:10.1007/978-1-4613-3315-9_28
- Cleveland, J. S., and Weidemann, A. D. (1993). Quantifying Absorption by Aquatic Particles: A Multiple Scattering Correction for Glass-Fiber Filters. *Limnol. Oceanogr.* 38, 1321–1327. doi:10.4319/lo.1993.38.6.1321
- Dall'olmo, G., and Gitelson, A. A. (2005). Effect of Bio-Optical Parameter Variability on the Remote Estimation of Chlorophyll-A Concentration in Turbid Productive Waters: Experimental Results. *Appl. Opt.* 44, 412–422. doi:10.1364/ao.44.000412
- Dall'olmo, G., and Gitelson, A. A. (2006). Effect of Bio-Optical Parameter Variability and Uncertainties in Reflectance Measurements on the Remote Estimation of Chlorophyll-A Concentration in Turbid Productive Waters: Modeling Results. *Appl. Opt.* 45, 3577–3592. doi:10.1364/ao.45.003577
- Dekker, A. G. (1993). *Detection of Optical Water Quality Parameters for Eutrophic Waters by High Resolution Remote Sensing*.
- Duan, H., Ma, R., Zhang, Y., Loisel, S. A., Xu, J., Zhao, C., et al. (2010). A New Three-Band Algorithm for Estimating Chlorophyll Concentrations in Turbid Inland Lakes. *Environ. Res. Lett.* 5, 044009. doi:10.1088/1748-9326/5/4/044009
- Feng, L., Hu, C., Han, X., Chen, X., and Qi, L. (2014). Long-Term Distribution Patterns of Chlorophyll-A Concentration in China's Largest Freshwater Lake: MERIS Full-Resolution Observations with a Practical Approach. *Remote Sensing* 7, 275–299. doi:10.3390/rs70100275
- Gitelson, A. A., Schalles, J. F., and Hladik, C. M. (2007). Remote Chlorophyll-A Retrieval in Turbid, Productive Estuaries: Chesapeake Bay Case Study. *Remote Sensing Environ.* 109, 464–472. doi:10.1016/j.rse.2007.01.016
- Gordon, H. R., Brown, O. B., Evans, R. H., Brown, J. W., Smith, R. C., Baker, K. S., et al. (1988). A Semianalytic Radiance Model of Ocean Color. *J. Geophys. Res.* 93, 10909–10924. doi:10.1029/jd093id09p10909
- Guanter, L., Ruiz-Verdú, A., Odermatt, D., Giardino, C., Simis, S., Estellés, V., et al. (2010). Atmospheric Correction of ENVISAT/MERIS Data over Inland Waters: Validation for European Lakes. *Remote Sensing Environ.* 114, 467–480. doi:10.1016/j.rse.2009.10.004
- Guo, Y., Huang, C., Zhang, Y., Li, Y., and Chen, W. (2020). A Novel Multitemporal Image-Fusion Algorithm: Method and Application to GOCI and Himawari Images for Inland Water Remote Sensing. *IEEE Trans. Geosci. Remote Sensing* 58, 4018–4032. doi:10.1109/tgrs.2019.2960322
- Gurlin, D., Gitelson, A. A., and Moses, W. J. (2011). Remote Estimation of Chl-A Concentration in Turbid Productive Waters - Return to a Simple Two-Band NIR-Red Model? *Remote Sensing Environ.* 115, 3479–3490. doi:10.1016/j.rse.2011.08.011
- Haardt, H., and Maske, H. (1987). Specific *In Vivo* Absorption Coefficient of Chlorophyll a at 675 Nm1. *Limnol. Oceanogr.* 32, 608–619. doi:10.4319/lo.1987.32.3.0608
- Honeywill, C., Paterson, D., and Hagerthey, S. (2002). Determination of Microphytobenthic Biomass Using Pulse-Amplitude Modulated Minimum Fluorescence. *Eur. J. Phycology* 37, 485–492. doi:10.1017/s0967026202003888
- Huang, C.-C., Li, Y.-M., Sun, D.-Y., and Le, C.-F. (2011). Retrieval of Microcystis Aetginosa Percentage from High Turbid and Eutrophia Inland Water: A Case Study in Taihu Lake. *IEEE Trans. Geosci. Remote Sensing* 49, 4090–4100. doi:10.1109/tgrs.2011.2129521
- Huang, C., Guo, Y., Yang, H., Li, Y., Zou, J., Zhang, M., et al. (2015a). Using Remote Sensing to Track Variation in Phosphorus and its Interaction with Chlorophyll-A and Suspended Sediment. *IEEE J. Sel. Top. Appl. Earth Observations Remote Sensing* 8, 4171–4180. doi:10.1109/jstars.2015.2438293
- Huang, C., Shi, K., Yang, H., Li, Y., Zhu, A.-X., Sun, D., et al. (2015b). Satellite Observation of Hourly Dynamic Characteristics of Algae with Geostationary Ocean Color Imager (GOCI) Data in Lake Taihu. *Remote Sensing Environ.* 159, 278–287. doi:10.1016/j.rse.2014.12.016
- Huang, C., Zou, J., Li, Y., Yang, H., Shi, K., Li, J., et al. (2014). Assessment of NIR-Red Algorithms for Observation of Chlorophyll-A in Highly Turbid Inland Waters in China. *ISPRS J. Photogrammetry Remote Sensing* 93, 29–39. doi:10.1016/j.isprsjprs.2014.03.012
- Kravitz, J., Matthews, M., Bernard, S., and Griffith, D. (2019). Application of Sentinel 3 OLCI for Chl-A Retrieval over Small Inland Water Targets: Successes and Challenges. *Remote Sensing Environ.* 237.
- Kutser, T. (2004). Quantitative Detection of Chlorophyll in Cyanobacterial Blooms by Satellite Remote Sensing. *Limnol. Oceanogr.* 49, 2179–2189. doi:10.4319/lo.2004.49.6.2179
- Le, C., Hu, C., English, D., Cannizzaro, J., Chen, Z., Feng, L., et al. (2013). Towards a Long-Term Chlorophyll-A Data Record in a Turbid Estuary Using MODIS Observations. *Prog. Oceanography* 109, 90–103. doi:10.1016/j.pocean.2012.10.002
- Le, C., Li, Y., Zha, Y., Sun, D., Huang, C., and Lu, H. (2009). A Four-Band Semi-analytical Model for Estimating Chlorophyll a in Highly Turbid Lakes: The Case of Taihu Lake, China. *Remote Sensing Environ.* 113, 1175–1182. doi:10.1016/j.rse.2009.02.005
- Le, C., Li, Y., Zha, Y., Sun, D., Huang, C., and Zhang, H. (2011). Remote Estimation of Chlorophyll a in Optically Complex Waters Based on Optical Classification. *Remote Sensing Environ.* 115, 725–737. doi:10.1016/j.rse.2010.10.014
- Lee, Z., Lance, V. P., Shang, S., Vaillancourt, R., Freeman, S., Lubac, B., et al. (2011). An Assessment of Optical Properties and Primary Production Derived from Remote Sensing in the Southern Ocean (SO GasEx). *J. Geophys. Res. Oceans* 116, 1978–2012. doi:10.1029/2010jc006747
- Li, J. (2007). *Study of Retrieval of Inland Water Quality Parameters from Hyperspectral Remote Sensing Data by Analytical Approach - Taking Taihu Lake as an Example [doctor's Thesis]*. [Beijing: Institute of Remote Sensing Application, Chinese Academy of Sciences.
- Li, Y., Huang, J., Wei, Y., and Lu, W. (2006). Inverting Chlorophyll Concentration of Taihu Lake by Analytic Model. *J. Remote Sensing* 10, 169–175.
- Liu, G., Li, L., Song, K., Li, Y., Lyu, H., Wen, Z., et al. (2020). An OLCI-Based Algorithm for Semi-empirically Partitioning Absorption Coefficient and Estimating Chlorophyll a Concentration in Various Turbid Case-2 Waters. *Remote Sensing Environ.* 239, 111648. doi:10.1016/j.rse.2020.111648
- Liu, G., Li, Y., Lyu, H., Wang, S., Du, C., and Huang, C. (2015). An Improved Land Target-Based Atmospheric Correction Method for Lake Taihu. *IEEE J. Selected Top. Appl. Earth Observations Remote Sensing* 9, 793–803.
- Morel, A., and Gentili, B. (1993). Diffuse Reflectance of Oceanic Waters II Bidirectional Aspects. *Appl. Opt.* 32, 6864–6879. doi:10.1364/ao.32.006864
- Moses, W. J., Gitelson, A. A., Berdnikov, S., Bowles, J. H., Povazhnyi, V., Saprygin, V., et al. (2014). *HICO-based NIR-Red Models for Estimating Chlorophyll-Concentration in Productive Coastal Waters*.
- Moses, W. J., Gitelson, A. A., Perk, R. L., Gurlin, D., Rundquist, D. C., Leavitt, B. C., et al. (2012). Estimation of Chlorophyll-A Concentration in Turbid Productive Waters Using Airborne Hyperspectral Data. *Water Res.* 46, 993–1004. doi:10.1016/j.watres.2011.11.068
- Mueller, J. L., Morel, A., Frouin, R., Davis, C., Arnone, R., Carder, K., et al. (2003). *Ocean Optics Protocols for Satellite Ocean Color Sensor Validation, Revision 4. Volume III: Radiometric Measurements and Data Analysis Protocols*.
- Neil, C., Spyarakos, E., Hunter, P. D., and Tyler, A. N. (2019). A Global Approach for Chlorophyll-A Retrieval across Optically Complex Inland Waters Based on Optical Water Types. *Remote Sensing Environ.* 229, 159–178. doi:10.1016/j.rse.2019.04.027
- Palmer, S. C. J., Odermatt, D., Hunter, P. D., Brockmann, C., Présing, M., Balzter, H., et al. (2015). Satellite Remote Sensing of Phytoplankton Phenology in Lake Balaton Using 10years of MERIS Observations. *Remote Sensing Environ.* 158, 441–452. doi:10.1016/j.rse.2014.11.021
- Shi, K., Li, Y., Li, L., Lu, H., Song, K., Liu, Z., et al. (2013). Remote Chlorophyll-A Estimates for Inland Waters Based on a Cluster-Based Classification. *Sci. Total Environ.* 444, 1–15. doi:10.1016/j.scitotenv.2012.11.058
- Smyth, T. J., Moore, G. F., Hirata, T., and Aiken, J. (2006). Semianalytical Model for the Derivation of Ocean Color Inherent Optical Properties: Description, Implementation, and Performance Assessment. *Appl. Opt.* 45, 8116–8131. doi:10.1364/ao.45.008116
- Tang, J., Tian, G., Wang, X., Wang, X., and Song, Q. (2004). The Method of Water Spectra Measurement and Analysis I: Above-Water Method. *J. Remote Sensing* 8, 37–44.
- Xu, J., Li, F., Zhang, B., Song, K., Wang, Z., Liu, D., et al. (2009). Estimation of Chlorophyll-A Concentration Using Field Spectral Data: a Case Study in Inland Case-II Waters, North China. *Environ. Monit. Assess.* 158, 105–116. doi:10.1007/s10661-008-0568-z

- Yacobi, Y. Z., Moses, W. J., Kaganovsky, S., Sulimani, B., Leavitt, B. C., and Gitelson, A. A. (2011). NIR-red Reflectance-Based Algorithms for Chlorophyll-A Estimation in Mesotrophic Inland and Coastal Waters: Lake Kinneret Case Study. *Water Res.* 45, 2428–2436. doi:10.1016/j.watres.2011.02.002
- Yang, W., Matsushita, B., Chen, J., Fukushima, T., and Ma, R. (2010). An Enhanced Three-Band index for Estimating Chlorophyll-A in Turbid Case-II Waters: Case Studies of Lake Kasumigaura, Japan, and Lake Dianchi, China. *IEEE Geosci. Remote Sensing Lett.* 7, 655–659. doi:10.1109/lgrs.2010.2044364
- Zhang, Y., Ma, R., Duan, H., Loisel, S., and Xu, J. (2014). A Spectral Decomposition Algorithm for Estimating Chlorophyll-A Concentrations in Lake Taihu, China. *Remote Sensing* 6, 5090–5106. doi:10.3390/rs6065090
- Zimba, P. V., and Gitelson, A. (2006). Remote Estimation of Chlorophyll Concentration in Hyper-Eutrophic Aquatic Systems: Model Tuning and Accuracy Optimization. *Aquaculture* 256, 272–286. doi:10.1016/j.aquaculture.2006.02.038

Conflict of Interest: The authors declare that the research was conducted in the absence of any commercial or financial relationships that could be construed as a potential conflict of interest.

Publisher's Note: All claims expressed in this article are solely those of the authors and do not necessarily represent those of their affiliated organizations, or those of the publisher, the editors and the reviewers. Any product that may be evaluated in this article, or claim that may be made by its manufacturer, is not guaranteed or endorsed by the publisher.

Copyright © 2022 Guo, Huang, Li, Du, Li, Chen, Shi and Ji. This is an open-access article distributed under the terms of the Creative Commons Attribution License (CC BY). The use, distribution or reproduction in other forums is permitted, provided the original author(s) and the copyright owner(s) are credited and that the original publication in this journal is cited, in accordance with accepted academic practice. No use, distribution or reproduction is permitted which does not comply with these terms.

APPENDIX A

The total absorption a and backscattering coefficients b_b were modeled as the sum of absorption and backscattering from water constituents, as follows:

$$a(\lambda) = a_d(\lambda) + a_{ph}(\lambda) + a_{CDOM}(\lambda) + a_w(\lambda) \quad (A1)$$

$$b_b(\lambda) = b_{bp}(\lambda) + b_{bw}(\lambda) \quad (A2)$$

where the subscripts d, ph, and w represent non-algal particle, phytoplankton, and pure water, respectively. $a_d(\lambda)$ and $a_{ph}(\lambda)$ can be parameterized using the following equations:

$$a_d(\lambda) = a_d^*(\lambda) \times C_{TSM} \quad (A3)$$

$$a_{ph}(\lambda) = a_{ph}^*(\lambda) \times C_{chl a} \quad (A4)$$

where $a_d^*(\lambda)$ and $a_{ph}^*(\lambda)$ are the specific absorption coefficients of non-algal particle and phytoplankton, respectively;

The absorption of CDOM can be parameterized by:

$$a_{CDOM}(\lambda) = a_{CDOM}(\lambda_0) \times \exp(-S(\lambda - \lambda_0)) \quad (A5)$$

where $a_{CDOM}(\lambda_0)$ is the absorption coefficient of CDOM at the reference wavelength λ_0 ; S is the CDOM absorption spectrum slope; λ_0 was set to 440 nm. S was set to 0.013 (Li et al., 2006). As CDOM don't make obvious contributions to the Red-NIR spectrum (Zhang et al., 2014), in this study, the sensitivity of $C_{chl a}$ models to a_{CDOM} was not discussed. $a_{CDOM}(\lambda_0)$ is set to 0.5.

The backscattering coefficients of non-algal particle can be parameterized using the following equation:

$$b_{bp}(\lambda) = b_p^*(\lambda) \times C_{TSM} \times \tilde{b}_p \quad (A6)$$

where $b_p^*(\lambda)$ and \tilde{b}_p are the specific coefficients and backscattering probability of non-algal particle. In this study, \tilde{b}_p is set to 0.05 (Li, 2007). The backscattering probability of pure water is 0.5. $a_d^*(\lambda)$, $a_{ph}^*(\lambda)$ and $b_p^*(\lambda)$ were from Dall'olmo and Gitelson, 2006 (Huang et al., 2011) research. The simulation was processed combing Eqs. A1–A6, and (3).